processes

MDPI

Article

Design and Characterization of a Melt Electrostatic Precipitator for Advanced Drug Formulations

Anna Justen, Alina Faye Weltersbach, Gerhard Schaldach and Markus Thommes *

Laboratory of Solids Process Engineering, Department of Biochemical and Chemical Engineering, Technical University Dortmund, Emil-Figge-Straße 68, 44227 Dortmund, Germany
* Correspondence: professors.fsv.bci@tu-dortmund.de; Tel.: +49-2317556988

Abstract: Electrostatic precipitators (ESP) are especially known for the efficient separation of micron and submicron particles from aerosols. Wet electrostatic precipitators are particularly suitable for highly resistive materials. Using these, particles can be directly transferred into a liquid for further processing or safer handling, which is advantageous for either hazardous or valuable materials. In this work, a wet ESP, which enables the separation of highly resistive particles into a heated liquid, was designed and investigated. To do this, spray-dried drug particles were embedded in a molten sugar alcohol to enhance the drug dissolution rate. After cooling, the solidified product showed advantageous properties such as a high drug dissolution rate and easy handling for further processing. For the design of the wet ESP, different discharge electrode configurations were tested. A wall film served as the collection electrode, which was generated by a specially designed distributer die. A laminar flow regime was achieved with a homogeneous film serving as the collection electrode, which is particularly important for a high separation efficiency. A prototype was designed and constructed in this respect. The particle separation into hot liquids or onto hot surfaces is challenging due to thermal effects in ESPs. The influence of thermophoresis and drag force on the particle transport was investigated, and optimum operation parameters were found for the present ESP. A broad field of applications can be covered with the presented device, where particles are embedded in even hot liquids to form liquid suspensions or, as it is presented here, solid dispersions. The dissolution of the drug-containing solid dispersion was studied in vitro. A remarkably faster drug dissolution was observed from the solid dispersion, as compared to a powder mixture of the drug and xylitol.

Keywords: electrostatic precipitation; wall film; thermophoresis; solid dispersion; drug dissolution

Citation: Justen, A.; Weltersbach, A.F.; Schaldach, G.; Thommes, M. Design and Characterization of a Melt Electrostatic Precipitator for Advanced Drug Formulations. *Processes* **2024**, *12*, 100. https://doi.org/10.3390/pr12010100

Academic Editor: Haiping Zhu

Received: 8 December 2023
Revised: 24 December 2023
Accepted: 28 December 2023
Published: 1 January 2024

1. Introduction

Small particles are of great interest in different fields due to their high specific surface area and the associated beneficial properties like high reactivity and solubility. The collection of micron and submicron particles in electrostatic precipitators is highly efficient compared to other separators, and is the preferred method for cleaning air, due to its low pressure drop and robustness [1,2].

Electrostatic precipitators (ESP) can be operated as dry ESP, where a metal plate serves as the collection electrode, upon which a particle layer is built up during precipitation. They are suitable for materials with a resistivity in the range of 10^4–10^{10} Ωcm [2]. Materials with lower resistivity tend to lose particles of the layer due to so called re-entrainment. Particle layers of high resistivity (>10^{12} Ωcm) at the collecting electrode cause a voltage drop inside the layer and thus lead to back corona effects [3,4]. These particles are preferably processed in wet ESPs. In this case, a water film flows along the collecting electrode, which traps the particles and washes them away from the surface. This leads to higher separation efficiencies, especially in the submicron range [5,6]. One main challenge of wet ESPs is the uniform distribution of a water film along the collecting electrode [7]. Unevenly distributed

water streams form water-free regions on the collecting electrodes, resulting in a decrease of the separation efficiency and particle agglomeration on the dry spots [7].

A homogeneous corona current distribution over the collecting electrode increases the collection efficiency. Furthermore, small particles are mainly collected in regions of high corona current [8]. In order to obtain a homogenous electric field with uniformly distributed corona current, a wall film with a constant thickness is required. Variations in wall film thickness lead to differences in electric resistivity, and thus particle agglomeration, resulting in a dip in collection efficiency. Generally, the generation of a uniform wall film with low-viscosity fluids like water is challenging, but an even distribution of the wall film was found to be critical for high separation efficiencies [7]. Therefore, research has been conducted aiming at achieving a uniform distribution of a wall film over the collecting electrode. Membrane-collecting electrodes showed improved wetting behavior and separation efficiency [9]. Higher corona current density was observed than in wet ESPs with plain collecting electrodes, allowing for higher separation efficiencies [5–7].

Film thickness measurements of water wall films were found to be difficult, with significant fluctuations over the length of the collecting electrode [10]. Although particle separation efficiency is influenced by the characteristics of the wall film, film thickness measurements and a uniform film distribution in wet ESPs have not been a focus. The purpose of this study was the collection of particles in the wall film fluid. Therefore, attention was given only to the wall film generation and investigation of its thickness and uniformity.

As the realization of a uniform wall film is complex, devices for direct particle introduction into a liquid have been described in literature. Dey et al. designed a wet ESP for the manufacturing of nanosuspensions. A horizontal collection electrode covered with sodium chloride solution was used for gentle precipitation of different organic nanoparticles. The prevention of particle agglomeration was found to be a major advantage of the direct collection of nanoparticles in a liquid [11].

Anderlohr et al. developed a wet ESP for direct formation of aqueous suspensions [12]. Silicium dioxide particles were used as model substance. A single-stage, tube-style wet ESP was designed, where water is distributed tangentially with nozzles. Thereby an entirely covered electrode was assumed, but was not verified [13]. The particle size distribution of the obtained suspensions was measured with a scanning mobility particle sizer after redispersion of the suspension into an aerosol. Particle size distributions in the redispersed suspension were found to be similar to those of the aerosol.

Another parameter in ESPs which should be considered carefully is the temperature. The influence of gas temperature on ESP efficiency was intensively studied. It is known that increased temperature leads to a decrease in corona inception and spark over voltage, and an increase of corona current [2,14]. Furthermore, the temperature of the collection electrode, or in the case of wet ESPs, the wall film temperature, also influences the particle collection characteristics. The temperature of wall films was either kept at room temperature [11,12] or cooled for enhanced particle deposition [15]. The physical phenomenon taken advantage of thereby is thermophoresis. It is described as the particle migration in a fluid induced by a temperature gradient, whereby the particle movement is directed away from high temperatures. It was found that thermophoresis could enhance particle deposition into cold water films [15,16]. Many theoretical studies were conducted investigating the particle deposition due to combined electrostatic and thermophoretic effects [17–20], but little experimental data is available [15,16,21]. Moreover, the particle deposition characteristics with a heated wall film have not been investigated in literature so far.

In previous studies, a melt electrostatic precipitator with a horizontal collection electrode covered with molten xylitol was presented. Drug particles were deposited onto the hot xylitol and an increased drug dissolution was found [22]. Nevertheless, the process time was found to be limited by the built up particle layer on the xylitol melt due to back corona effects [23].

To overcome this limitation, in this study, a new electrostatic precipitator for direct particle deposition in a heated wall film is presented. Thereby, drug particles were embedded in the molten sugar alcohol, xylitol. The final solid product contains fine dispersed particles in a crystallized carrier material. These solid dispersions are used in pharmaceutical technology to improve the dissolution of a poorly water-soluble drug [22,24]. However, the presented prototype can be used for various applications, where particles are separated from gas streams, and a direct embedding into a liquid is required.

A liquid distributer for the generation of a uniform wall film was designed and its film thickness and uniformity were investigated experimentally. Generally, the particle deposition towards heated wall films in the presence of an electric field is rather complex and has not been investigated yet. The effect of a temperature gradient lowering the particle deposition had to be overcome and was investigated in the present study. Furthermore, the product was studied with respect to the in vitro dissolution behavior.

2. Materials and Methods

2.1. Materials

Celecoxib (Hangzhou Yuhao Chemical Technology, Wuhan, China) was used as the model drug substance to analyze the amount of drug particles which were collected on the heated collection electrode wall and in the wall film. It was chosen based on its UV traceability and high solubility in acetone for high particle mass load in the aerosol. Moreover, celecoxib has a high resistivity of about 4.5×10^{13} Ωcm [23], which was considered to be particularly challenging in the ESP due to the back corona.

Molten xylitol and an 83 wt.% glycerol–water mixture (Carl-Roth, Karlsruhe, Germany) were used as liquids to generate a laminar wall film. Film thickness measurements were conducted with the 83 wt.% glycerol–water mixture. Particle embedding was analyzed with molten xylitol (Roquette, Lestrem, France).

2.2. Methods

2.2.1. Spray Drying

A custom-made spray dryer was used to generate particles [23]. An aqueous or acetone solution was nebulized with an ultrasonic atomizer operating at a high frequency of 3.2 MHz. The gas-borne droplets were dried and the resulting particles were transported into the electrostatic precipitator. For calculations of the precipitation chamber dimensions, particles with a median volume-based diameter ($d_{50,3}$) of 2 µm with a high submicron share according to a previous study [23] were assumed.

2.2.2. Electrostatic Precipitator

A single-stage wet electrostatic precipitator was designed and constructed. The particle-laden aerosol was directed through a diffuser in order to guarantee a laminar inflow in the charging and precipitation zone. The precipitation chamber had a length of 200 mm and a width of 150 mm.

In a stainless steel frame, tungsten wires with a diameter of 0.2 mm were mounted over a length of 200 mm to serve as the discharge electrode. A small discharge electrode diameter was chosen due to a higher emitted corona current and a lower corona inception voltage, which is attributed to an increased electric field strength in the surrounding of the wire [25] as compared to higher diameters [26–28]. A multi-wire discharge electrode is known to provide higher corona current and thereby higher collection efficiency on the one hand [27,29,30], but it can also lead to opposite effects due to corona shielding [25]. In order to identify the optimum discharge electrode design, current-voltage characteristics were determined. Up to 5 parallel wires were used with a minimum tested distance between each wire of 10 mm. Tungsten was chosen due to its high melting point, stability against oscillations during high voltage application (attributed to the comparably high modulus of elasticity [31]), and a convenient work function [32].

The discharge and collecting electrode had a distance of 50 mm. A wall film served as the collection electrode, which spread over an area of 200 × 100 mm. In order to guarantee a laminar wall film with a uniform distribution of liquid over the length of 200 mm, a distributer was designed. The construction was based on extrusion flat slit dies. A so-called coat hanger manifold was chosen due to its reliable, uniform liquid distribution.

2.2.3. Current-Voltage Characteristics

The current-voltage characteristic was studied without a continuous wall film and at room temperature. A tungsten wire of 0.2 mm diameter served as discharge electrode, while the number and distance of wires was varied. A high-voltage generator was used (PNC 20000-30 ump, Heinzinger, Rosenheim, Germany) to apply a negative voltage up to 20 kV to the discharge electrode. To record the corona current, a stainless steel plate was placed in front of the collection electrode with an area of 200 cm^2. An ammeter (UT171 Series, Unitrend Technology, Dongguan City, China) was mounted between the stainless steel plate and a grounding wire. With this arrangement, an exact measurement of the corona current was possible, as current flow through the electrostatic precipitator walls and pipes was not measured.

2.2.4. Wall Film Thickness

The film thickness of a wall film and the flow regime mainly depend on the liquid's properties of viscosity, density and surface tension [33]. In order to adjust a volume flow for the laminar regime and to construct a coat-hanger distributer, liquid properties were determined for molten xylitol and an 83 wt.% glycerol-water mixture. An 83 wt.% glycerol-water mixture was chosen as a model liquid due to its similar properties at room temperature to molten xylitol (see Table 1). Investigations of the wall film thickness and film spreading could therefore be conducted in an experimental setup without heating. The liquid properties were determined with a rheometer (Haake Mars 60, Thermo Fisher Scientific, Karlsruhe, Germany) (viscosity) and hanging drop method (OCA 15EC, Dataphysics, Filderstadt, Germany) (surface tension).

Table 1. Measured liquid properties.

Liquid	Dynamic Viscosity [mPas]	Density [kg/m^3]	Surface Tension [mN/m]
glycerol-water mixture 83 wt.%	90	1217	54
molten xylitol (120 °C)	90	1311	48

The experimental setup a consisted of a coat-hanger distributer, which was 3D printed from polylactide, according to the design described in Section 3.1. It was mounted to a stainless steel plate with the same dimensions as the collection electrode in the electrostatic precipitator. Volume flows between 260 mL/min and 1100 mL/min were tested using a gear pump (Ismatec, MS Reglo 183, Wertheim, Germany). For film thickness measurements, a device for confocal, chromatic thickness measurement (CHRocodile S, Precitec Optronik, Gaggenau-Bad Rotenfels, Germany) was used.

2.2.5. Dry Precipitation

For particle embedding, the molten sugar alcohol, xylitol, was used, the melting temperature of which is 96 °C [34]. Therefore, the collecting electrode was heated throughout the process. It is known that if a fluid can move freely in a confined space, a motion directed away from warm surfaces and towards areas of equal temperature can be observed [35]. Therefore, the influence of the temperature gradient between the inlet aerosol and collection electrode on the particle collection was investigated.

The electrostatic precipitator was operated without a wall film; thus, particles were precipitated at the plain collection electrode. Therefore, a 60 g/L solution of celecoxib

in acetone was spray-dried and a carbon dioxide volume flow of 3 L/min was adjusted to transport the particles into the precipitation chamber. The aerosol temperature was measured at the beginning of the charging zone and adjusted by a heating section just before the electrostatic precipitator. Two field strengths were tested by adjusting the applied voltage. After a precipitation of 30 min, the particle layer, which was built up on the collection electrode, was removed with acetone and caught in a glass beaker. The acetone was evaporated at 60 °C for 4 h, and the remaining celecoxib mass was quantified.

2.2.6. Wet Precipitation

An aerosol with a celecoxib particle mass flow of 0.08 g/min was generated out of an acetone solution. A wall film of molten xylitol served as collecting electrode, which was pumped in a loop with a gear pump (GM601D-30R-110Z, Barmag, Remscheid, Germany). The celecoxib particles were continuously deposited into the xylitol melt over a period of 8 h. The collected celecoxib mass was quantified by a UV spectrometer (Biomate 3, Thermo Fisher Scientific, Waltham, MA, USA) at 256 nm in an isopropyl alcohol–water mixture (50% v/v).

2.2.7. Product Characterization

After wet precipitation, the drug-laden xylitol melt was cooled at room temperature and a solid product was obtained (solid dispersion). It was characterized regarding its dissolution behavior. Specifically, the in vitro dissolution was studied with the apparatus 4 (flow-through-cell), according to the procedure described in the European Pharmacopoeia [36]. Purified water was heated to 37 °C and a flow rate of 16 mL/min was adjusted with a gear pump (Ismatec, MS Reglo 183, Wertheim, Germany). The absorption of celecoxib was continuously monitored in a UV/Vis spectrometer (Lambda2S, Perkin Elmer, Überlingen, Germany) at a wavelength of 250 nm. In addition to the solid dispersion obtained with the melt electrostatic precipitator, a physical mixture with comparable drug content (0.5 wt.%) was prepared with a 3D tumbler mixer (Turbula T10B, Willy A. Bachofen AG, Muttenz, Switzerland). The drug dissolution measurements were conducted under sink conditions (1/10 c_s).

3. Results and Discussion

3.1. Design and Construction

3.1.1. Liquid Distributer Design

In order to create a laminar, waveless wall film, a die was designed based on the concept of flat-slit extrusion dies, consisting of a manifold or flow channel and a land area. For the construction, an incompressible fluid with a constant viscosity in the entire die as well as an isothermal, laminar flow, were assumed. The design of a coat-hanger die was chosen as it provides a more stable, uniform melt distribution compared to the fishtail or T-die. However, its construction is more complex, as the manifold radius, R, constricts in the flow direction in order to obtain equal flow velocities, v_{die}, in the entire die [37]. The manifold radius with respect to position along the flow direction (x) can be described as follows:

$$R(x) = R_{max}\left(\frac{x}{W}\right)^{\frac{1}{3}} \quad (1)$$

Similar to the manifold radius, the length of the land area can be calculated as

$$Y(x) = Y_{max}\left(\frac{x}{W}\right)^{\frac{2}{3}} \quad (2)$$

The die is symmetrical. Therefore, only half of the die is considered, and W is referred to as half of the width of the die. Y is the length of land area, i.e., the distance from the manifold to the edge of the die, and R is the radius of the manifold [37]. The die is made of

stainless steel and constructed of two identical parts, which are fixed with screws (Figure 1). The width h between the two parts defines the die opening.

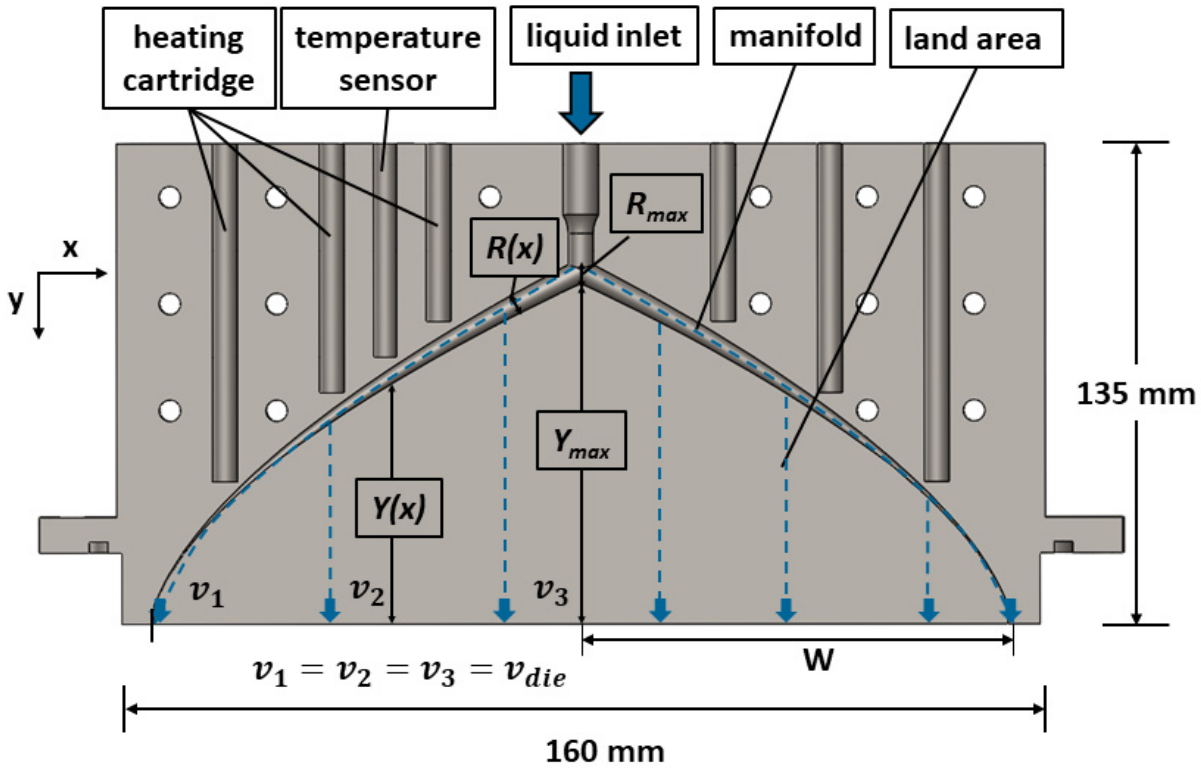

Figure 1. Schematic of liquid distributer.

In order to construct a versatile die geometry, constant shear rates in the manifold and land area were assumed. With this assumption, the following relation for maximum radius, R_{max}, results:

$$R_{max} = \left[\frac{2}{3\pi} \cdot W \cdot h^2\right]^{\frac{1}{3}} \quad (3)$$

where h is the opening width of the die [37]. The maximum length of the land area, Y_{max}, can thereby be calculated as

$$Y_{max} = \left(\frac{3}{2}\right)^{\frac{3}{4}} \cdot \left(\pi h W^2\right)^{\frac{1}{3}} \quad (4)$$

The height h of the die opening is set at 3 mm in order to guarantee a low film thickness, but also to avoid retention of liquid in the die. Since molten xylitol was used, spaces for heating cartridges and a temperature sensor were designed. In this way, both crystallization of the xylitol and clogging of the die was avoided.

3.1.2. Electrostatic Precipitator

For particle charging and precipitation, a wet electrostatic precipitator was designed, consisting of one precipitation chamber where a discharge electrode is mounted opposite to the collection electrode (wall film). The construction is based on previous theoretical considerations to ensure an efficient particle collection.

For a particle transport in an electric field, a corona inception at the discharge electrode, as indicated by a current flow, is necessary. The corona inception field strength, E_0, can

be determined by Peek's empirical equation for a wire discharge electrode and a plate collecting electrode [38]:

$$E_0 = C_1 \cdot \delta + C_2 \sqrt{\frac{\delta}{r_{de}}} \tag{5}$$

where r_{de} is the radius of the discharge electrode wire, C_1 and C_2 are empirical gas constants determined for air and negative corona [39], and δ is the gas density, which is described as

$$\delta = \frac{p \cdot T_0}{p_0 \cdot T} \tag{6}$$

with T_0 = 273 K and p_0 = 101,300 Pa.

From the field strength, E_0, a minimum voltage, or corona inception voltage, U_0, can be determined [28] to ensure the operating range (<20 kV) of the high voltage power supply used is not exceeded:

$$U_0 = E_0 \cdot r_{de} \cdot ln\left(\frac{f}{r_{de}}\right) \tag{7}$$

The factor f depends on the distance between the electrodes, a_{ce}, and can be calculated for the dimensions of the present electrostatic precipitator as

$$f = \frac{2}{\pi} \cdot a_{ce} \tag{8}$$

A rather small distance between the discharge and collecting electrodes of 50 mm and 150 mm was set in order to design a laboratory scale electrostatic precipitator with a low corona onset voltage and high electrical field strength. To confirm the choice of appropriate dimensions, the collection efficiency, ξ, was determined for an aerosol with a low particle concentration according to the modified Deutsch equation by Matts and Öhnfeld [40]:

$$\xi = 1 - e^{-\left(\frac{v_m \cdot A_{ce}}{\dot{V}_g}\right)^{0.5}} \tag{9}$$

The area of the collection electrode, A_{ce}, was set at 0.02 m^2. The gas volume flow, $\dot{V}_g$, in the spray dryer was adjusted to the lowest feasible flow rate (3 L/min) in order to obtain a long residence time in the precipitation chamber. The migration velocity, v_m, of the particles can be calculated with the Stokes drag force and the Cunningham correction factor for submicron particles [2]:

$$v_m = \frac{Q_p \cdot E}{3 \cdot \pi \cdot \eta_g \cdot d_p} Cu \tag{10}$$

$$Cu = 1 + Kn\left[2.514 + 0.8e^{\left(\frac{-0.55}{Kn}\right)}\right] \text{ with } Kn = \frac{2\Lambda}{d_p} \tag{11}$$

Here, Kn is the Knudsen number, which depends on the mean free path of gas molecules Λ. For air and atmospheric pressure, the mean free path becomes 0.07 µm [2]. η_g is the dynamic viscosity of the gas and d_p is the particle diameter. The particle charge, Q_p, is given by Equation (12) [2], which depends on the charging time, t, and the characteristic charging time, τ. For the calculation of the migration velocity, the particle saturation charge, Q_{max}, was estimated with the median particle size of the collective (2 µm) [23] and the corona inception field strength, E_0 (Equation (5)). The saturation charge, Q_{max}, is defined by Equation (13) [41] with the permittivity of vacuum, $\varepsilon_0 = 8.85 \cdot 10^{-12}$ Fm^{-1}.

$$Q_p(t) = Q_{max} \frac{t}{t + \tau} \tag{12}$$

$$Q_{max} = \pi \cdot \varepsilon_0 \cdot p \cdot d^2 \cdot E \tag{13}$$

For small particles (d_p < 0.1 µm) diffusion charging is the dominant mechanism, whereby larger particles (d_p > 2 µm) are mainly affected by field charging. Both mechanisms act simultaneously in between the two regions. Thus, the saturation charge is modified with the Knudsen number by the empirical factor p [42] to allow an estimation of the saturated particle charge for the entire particle size range:

$$p = (1 + Kn)^2 + \left(\frac{2}{1 + Kn}\right)\left(\frac{\varepsilon_r - 1}{\varepsilon_r + 2}\right) \quad (14)$$

The factor, p, depends on the material property, ε_r, which is the relative permittivity of the particles. ε_r of solid drug substances has rarely been determined in the literature. Therefore, it was estimated to be 5 Fm^{-1} in accordance with other organic solids [43–45]. With these calculations, a separation efficiency of 99.9% could be estimated for drug particles between 0.01 and 10 µm.

The electrostatic precipitator was built of stainless steel, as it is robust and temperature resistant, which is especially beneficial for complex parts like the coat hanger distributer. All parts in contact with the liquid, such as the coat hanger distributer, the wall film wall, and the liquid funnel, can be heated by heating cartridges (Figure 2). In the case of molten xylitol (melting temperature 96 °C), the parts were kept at 100 °C in order to prevent the liquid from crystallizing during the process.

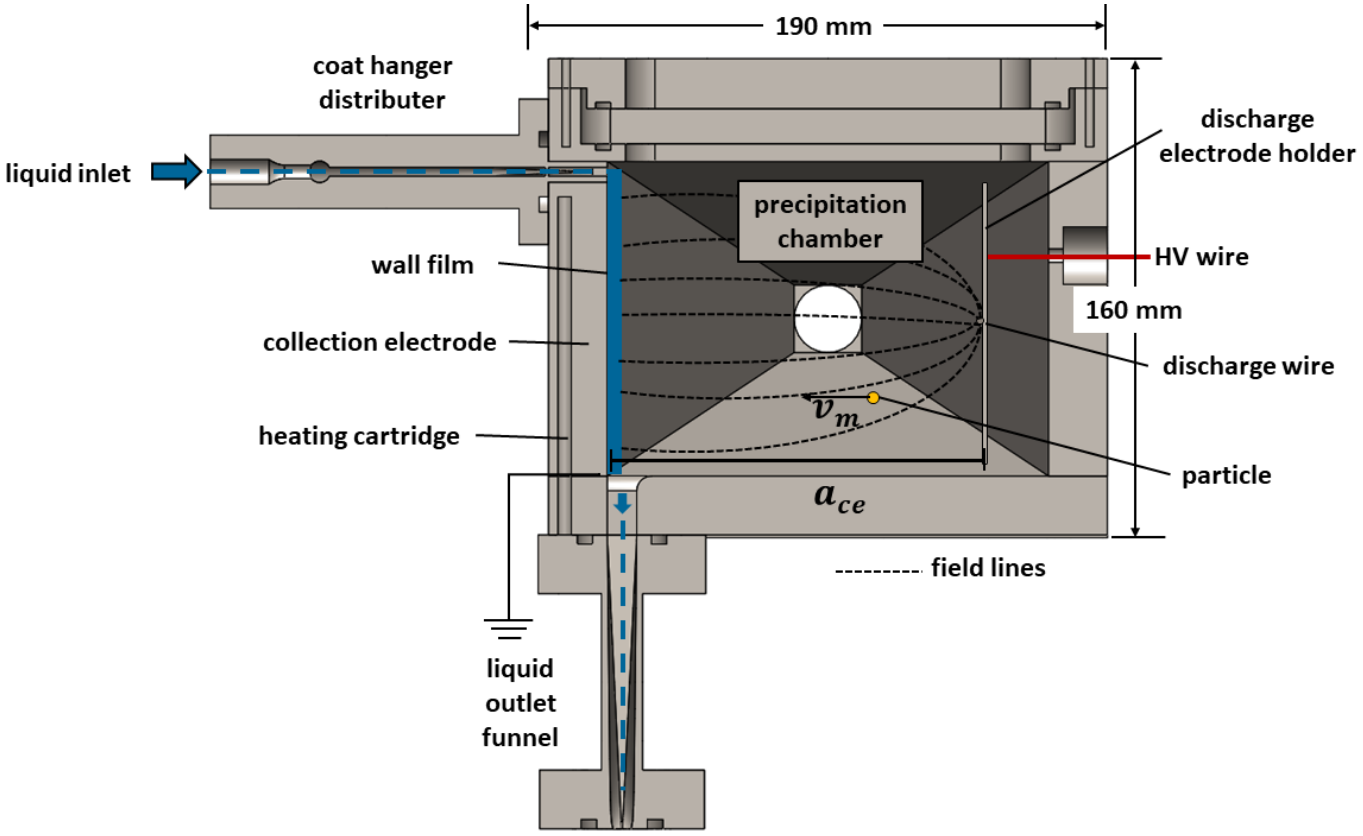

Figure 2. Schematic of cross-section of the precipitation chamber, with wall film as collection electrode (left), the liquid is depicted with blue arrows and lines. The discharge wire electrode is connected to a high voltage source (HV, red) (right).

The lid was made of glass to observe and control the precipitation process. To allow a laminar flow of the aerosol, an inlet and outlet diffuser were designed with an opening angle φ of 12° (Figure 3).

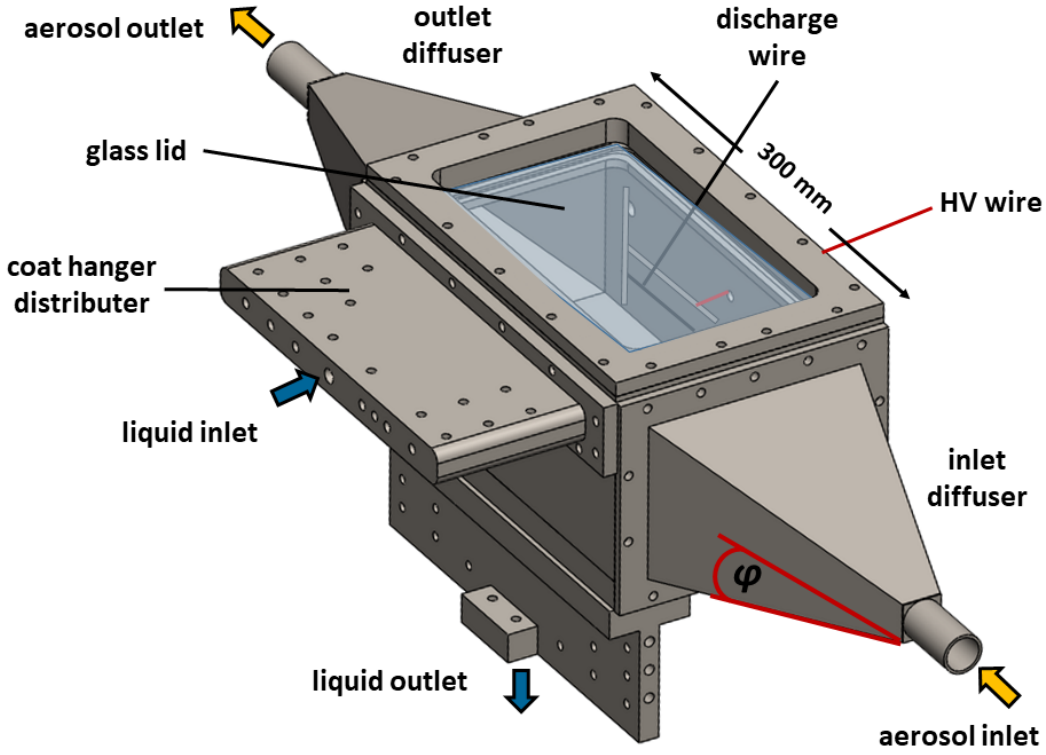

Figure 3. Schematic of electrostatic precipitator, completely assembled with glass lid, with diffuser opening angle φ.

3.2. Current-Voltage Characteristics

The current-voltage characteristics were measured for different electrode wire configurations in the "dry" electrostatic precipitator. In order to find the optimum discharge electrode configuration, up to 5 parallel wires were mounted in a stainless steel frame and the current density was measured for increasing applied voltage (Figure 4). A high corona current density should be generated in order to achieve a high particle separation.

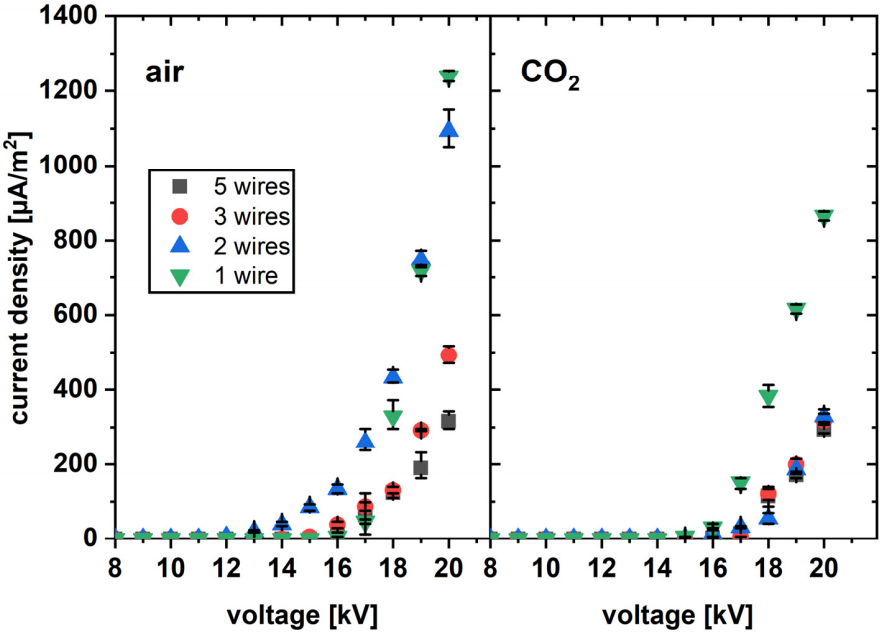

Figure 4. Measured current density at applied voltage with air and carbon dioxide as ionized gas and for up to 5 parallel mounted wires (av ± min/max, n = 3).

Carbon dioxide and air were used as ionizing gases. The wires were arranged in equal distance for each configuration. The distance between each wire was 80 mm, 40 mm and 20 mm for the 2-, 3- and 5-wire configuration, respectively.

The lowest corona onset voltage in air was found to occur for a 2-wire configuration. The highest current density was measured with a 1-wire configuration at 20 kV. The configurations with more than two wires showed a smaller slope and lower maximum current density. Overall, a higher current density was found for air than for carbon dioxide, as the ionization energy for carbon dioxide is high and the ion mobility is comparably low [46].

In carbon dioxide, the lowest corona onset voltage was measured with one wire, which also generated the highest current density at 20 kV. The maximum current density for more than one wire was limited to 300 $\mu A/m^2$, which is less than one third of the maximum obtained with one wire.

The observations were explained by the shielding effect, which is known to discharge electrodes that are in close vicinity [25]. As a high corona current facilitates high collection efficiencies, one wire was concluded to be the best configuration and was used for all further experiments.

3.3. Wall Film Characterization

The liquid distribution and flow regime in wet electrostatic precipitators have rarely been investigated in the literature. However, it was found that a uniform liquid distribution can increase the separation efficiency [7]. Therefore, an experimental setup was used to investigate the wall film spreading and thickness. An 83 wt.% glycerol-water mixture with similar properties to molten xylitol (see Table 1) was used. A polylactide die was 3D printed so that experiments could be conducted at room temperature without the use of heating equipment.

To characterize wall films, two dimensionless numbers were employed. The film Reynolds number Re (Equation (15)) and the inverse Kapitza, Ka, or film number, K_F (Equation (17)) [47]:

$$Re = \frac{\rho_f \cdot \Gamma}{\eta_f} \tag{15}$$

$$\Gamma = \frac{\dot{V}_f}{L} \tag{16}$$

$$K_F = \frac{1}{Ka} = \frac{g \cdot \eta_f^4}{\rho_f \cdot \sigma_f^3} \tag{17}$$

They depend on the fluid properties: dynamic viscosity,η_f, density, ρ_f, and surface tension, σ_f. The liquid load, Γ, can be calculated with the fluid volume flow, $\dot{V}_f$, and the length of the wall film, L.

Al-Sibai experimentally defined the flow regimens, where the critical Reynolds number for the smooth laminar regime, $Re_{crit,lam}$ is

$$Re_{crit,lam} = 0.6 \cdot K_f^{0.1} \tag{18}$$

Above $Re_{crit,lam}$, sinusoidal-shaped waves can be observed, which is indicated by a decreasing film thickness due to higher film velocity [48].

The average wall film thickness in the laminar and the wavy regime can be predicted by Equation (19), which was established by Nusselt [33]:

$$h = \left(\frac{3 \cdot \eta_f^2 \cdot}{g \cdot \rho_f^2} \right)^{\frac{1}{3}} \cdot Re^{\frac{1}{3}} \tag{19}$$

Figure 5 shows the average wall film thickness measured in 15 positions at different film Reynolds numbers. The film thickness increases with an increasing Reynolds number, whereby the prediction by Nusselt is suitable for this system in both the smooth laminar and the sinusoidal waves regime. The small error bars indicate small fluctuations over the entire wall film. The film thickness does not decrease beyond $Re_{crit,lam}$ as expected for sinusoidal waves. Nevertheless, higher fluctuations are observed.

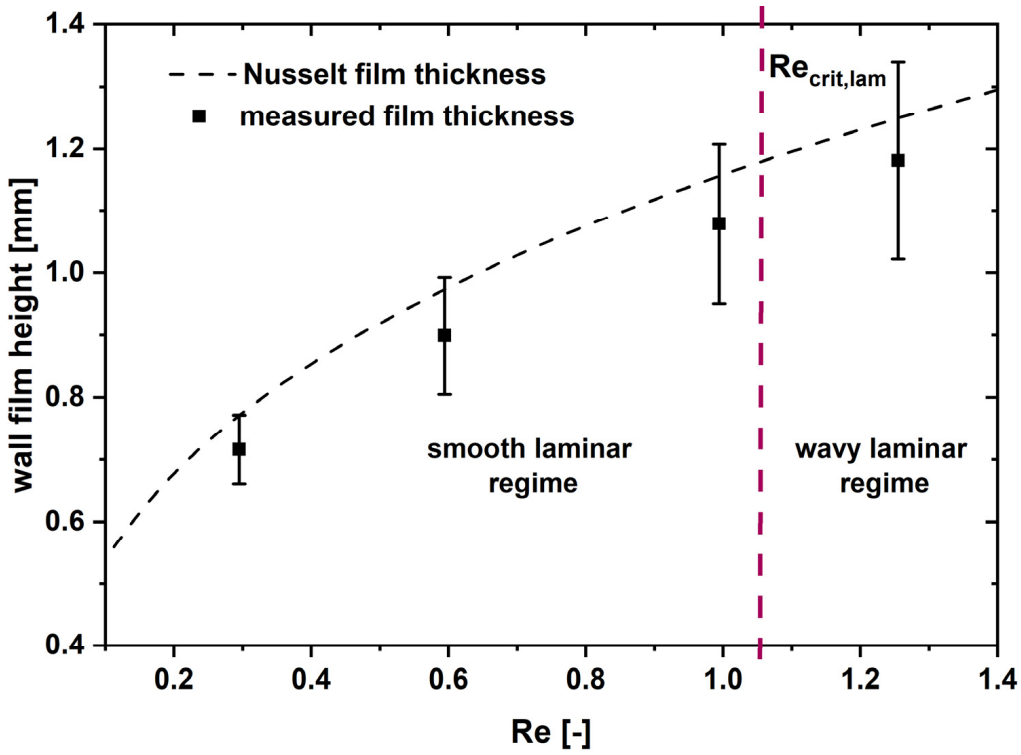

Figure 5. Average wall film thickness measured ■ and calculated --- (av ± s, n = 15).

Figure 6 shows the wall film thickness as a function of Reynolds number. An increasing film thickness with increasing volume flow was observed for each of the 15 measurement positions. Low deviations are observed except for position 1. For higher Reynolds numbers, the fluctuations at this position increase and cause the high standard deviations seen in Figure 6. These high fluctuations are assumed to be generated by surface deviations of the 3D printed model die. As the die in the final ESP is made of steel and the manifold and the island area were milled and polished, no surface irregularities should occur. For all further positions, almost no fluctuations were observed. A smooth laminar regime can be assumed, even for Reynolds numbers beyond $Re_{crit,lam}$.

The two crucial parameters for the generation of a wall film in a wet ESP are film spreading and film thickness. Dry spots on the collection electrode wall were found to decrease the separation efficiency [7] by disturbing the electric field and leading to back corona due to buildup of particle layers. Furthermore, a higher film thickness has a higher electric resistance, hence high fluctuations in film thickness lead to a non-uniform electric field and particle separation. Therefore, a smooth laminar flow regime was desired. Figures 5 and 6 confirm a uniform wall film over the entire wetted area. The designed coat hanger distributer was found to be a suitable device for the investigated range of Reynolds numbers, while the smooth laminar regime was identified even beyond the $Re_{crit,lam}$ by Al-Sibai [48].

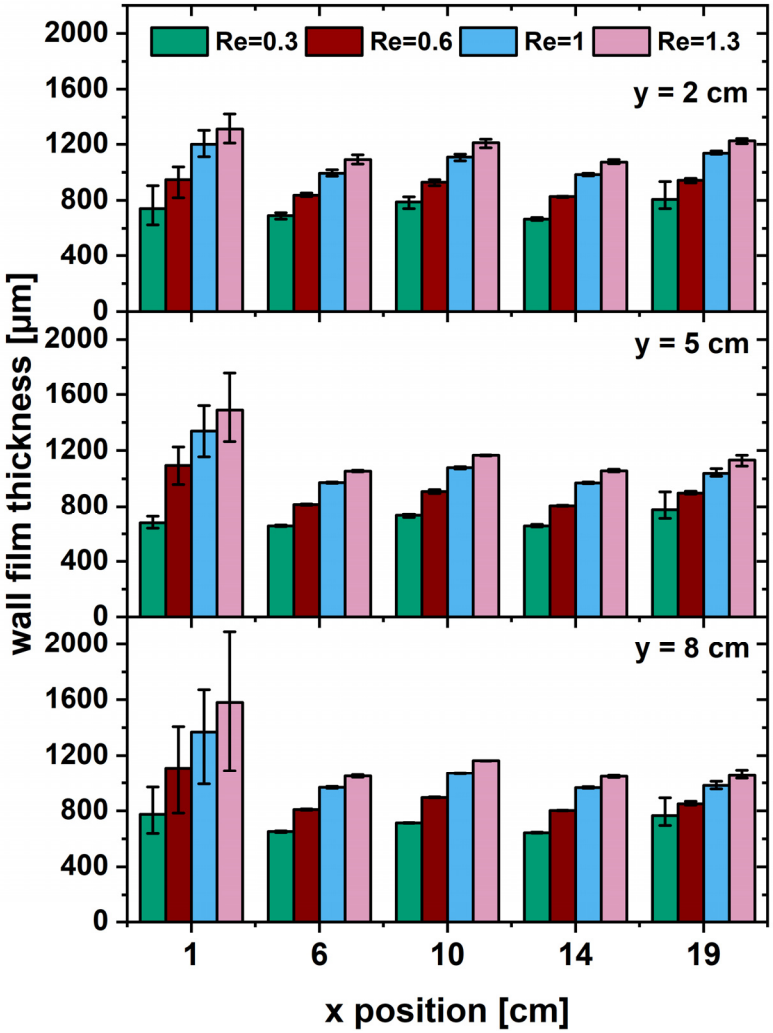

Figure 6. Wall film heights, measured in 5 positions in width (x direction) and 3 positions in height (y direction), where the y = 0 height would be the die opening (av ± min/max, n = 3).

3.4. Particle Deposition on a Hot Surface

One unique feature of the wet electrostatic precipitator presented in this study is the operation with a hot liquid. Next to the electrostatic force, F_E, the thermophoretic force, F_T, and drag force, F_D, also mainly affect the particle deposition. Their influence was investigated by quantification of the deposited particles on the plain, heated collection electrode (100 °C). Different aerosol temperatures were adjusted with an upstream aerosol heating section and measured in the center of the precipitation chamber (Figure 7).

With increasing aerosol temperature, the temperature gradient between the heated collection electrode (100 °C) and the aerosol temperature was minimized. Two regions of particle deposition behavior can be identified. In the first region, the deposition rate towards the wall increases with increasing aerosol temperature. The temperature gradient between the collection electrode wall and the aerosol is decreased. With lower field strength (55 kV m^{-1}), the particle deposition rate is lower than for the higher field strength.

Beyond a maximum, the deposition rate decreases as the temperature gradient decreases. The deposited particle amount for the investigated field strengths cannot be distinguished.

Generally, the electrostatic force, F_E, increases with an increasing electric field. High temperatures increase the drag force, F_D, leading to an upward flow of the aerosol.

The movement of particles in an aerosol away from warm surfaces is driven by the thermophoretic force, F_T [35]. With an increasing temperature gradient of a surface and a parallel flowing aerosol, F_T increases. Additionally, a thermal boundary layer forms along

the heated wall, leading to an upward-directed thermal convection flow along the wall due to the density gradient of the gas [49,50]. This boundary layer increases with an increasing temperature gradient between the gas with the temperature, T_∞, and the heated surface of temperature, T_w [49].

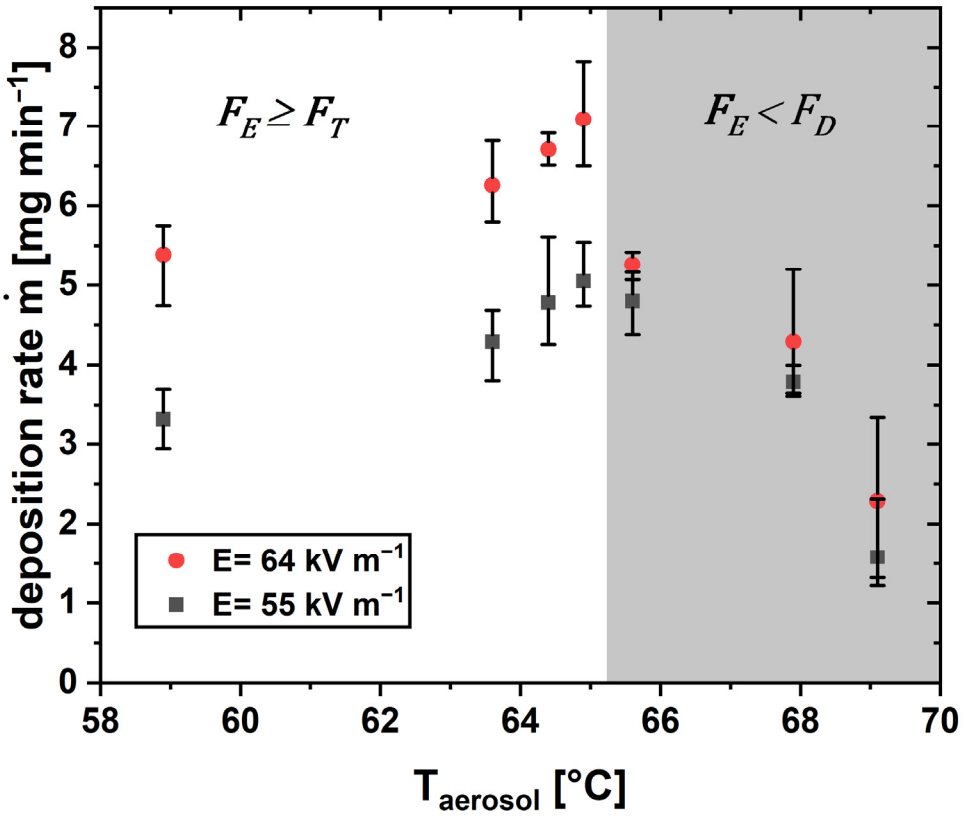

Figure 7. Deposition rate, $\dot{m}$, deposited on the heated collection electrode at different aerosol temperatures. The grey background marks the region, where the electrostatic force is minor. (av ± min/max, n = 3).

In the first region (59 °C and 65 °C aerosol temperature), the electrostatic force, F_E, dominates, as indicated by a higher mass flow rate for the higher field strength (64 kV m^{-1}). With a decreased temperature gradient, thermophoresis is reduced, and particles are transported by the electrostatic force towards the collection electrode. In addition, the transport of particles towards the collection electrode is less hindered by the boundary layer as its thickness decreases with decreasing temperature gradient.

The second region is characterized by a high influence of the drag force, F_D. It dominates the electrostatic force, F_E, so that the collection efficiency decreases [51,52]. No difference between the two applied field strengths can be identified, as the electrostatic force is not sufficient. Figure 8 shows a schematic of the forces acting on a particle in the ESP.

Two main factors hindering particle transport towards the collection electrode were identified. Firstly, thermophoresis caused particle movement away from the heated collecting electrode. Due to the temperature gradient, a thermal boundary layer developed. This boundary layer limited particle deposition due to a heat flux, $\dot{q}$, directed in the opposite direction of the electrostatic force. Secondly, an increase in aerosol temperatures led to an increasing drag force and thereby a decrease in deposition rate. Generally, high temperatures in ESPs are known to reduce collection efficiency due to increased electric wind, elevated drag force, and decreased electrostatic force [52].

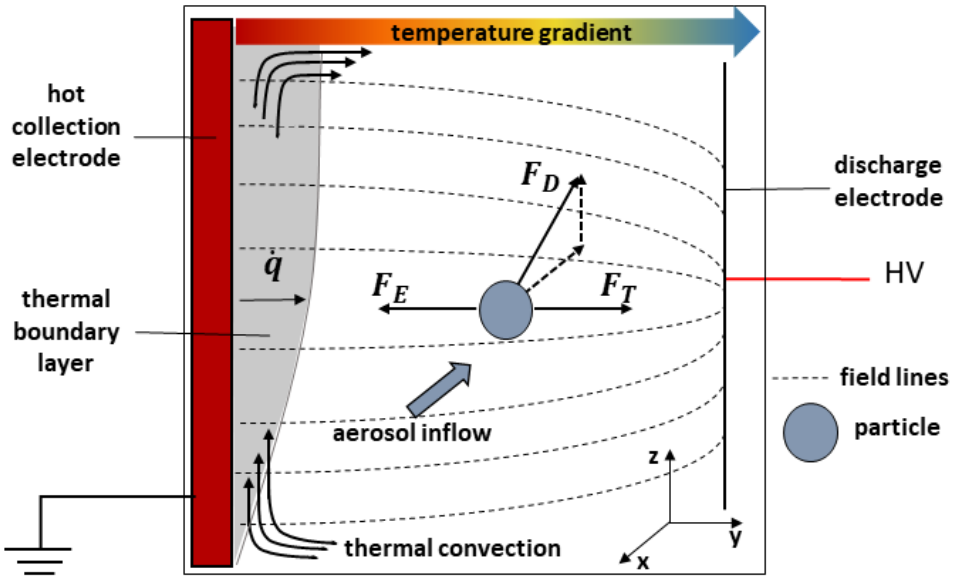

Figure 8. Schematic of the main forces, F_E (electrostatic), F_D (drag) and F_T (thermophoretic) acting on a particle in an ESP with a hot collecting electrode, while F_D results from the aerosol inflow in −x direction and the thermal convection in +z direction.

Assuming a thermal boundary layer at the collection electrode with a heat flux in the layer directed oppositely to the temperature gradient, the heat flux, $\dot{q}$, is defined as [53]

$$\dot{q} = -\alpha \cdot (T_w - T_\infty) \tag{20}$$

The heat transfer coefficient, α, can be calculated with the mean Nusselt number, Nu_m, the thermal conductivity, λ, of the gas forming the boundary layer and the characteristic length, l, which is the height of the heated wall where the boundary layer occurs [53].

$$\alpha = \frac{Nu_m \cdot \lambda}{l} \tag{21}$$

The mean Nusselt number describes the heat transfer by convection between a surface and a liquid over the boundary layer and depends on the Grashof number, Gr, and the Prandtl number, Pr [53].

$$Nu_m = \frac{0.901 \cdot Pr^{\frac{1}{2}}}{(0.861 + Pr)^{\frac{1}{4}}} \cdot \left(\frac{Gr}{4}\right)^{\frac{1}{4}} \tag{22}$$

The Grashof number is a dimensionless number, which is used to describe thermally induced convective flow:

$$Gr = \frac{\beta_\infty \cdot (T_w - T_\infty) \cdot g \cdot l^3}{\nu_f^2} \tag{23}$$

The coefficient of thermal expansion, β_∞, for an ideal gas is $\beta_\infty = 1/T_\infty$. The characteristic length, l, is the height of the heated wall, ν_f is the kinematic viscosity of the fluid, and g is the gravitational acceleration [53].

The Prandtl number, Pr, is defined as the relationship between kinematic viscosity and the thermal conductivity, a, of the fluid:

$$Pr = \frac{\upsilon_f}{a} \tag{24}$$

Figure 9 shows the deposition rate, $\dot{m}$, as a function of the heat flux, $\dot{q}$, for the region, where the thermophoretic force is the main limiting factor for particle transport.

The deposition rate towards the collection electrode increases with decreasing heat flux. With higher field strength, the deposited mass flow rate increases, as the thermal boundary layer decreases in an applied electric field [19].

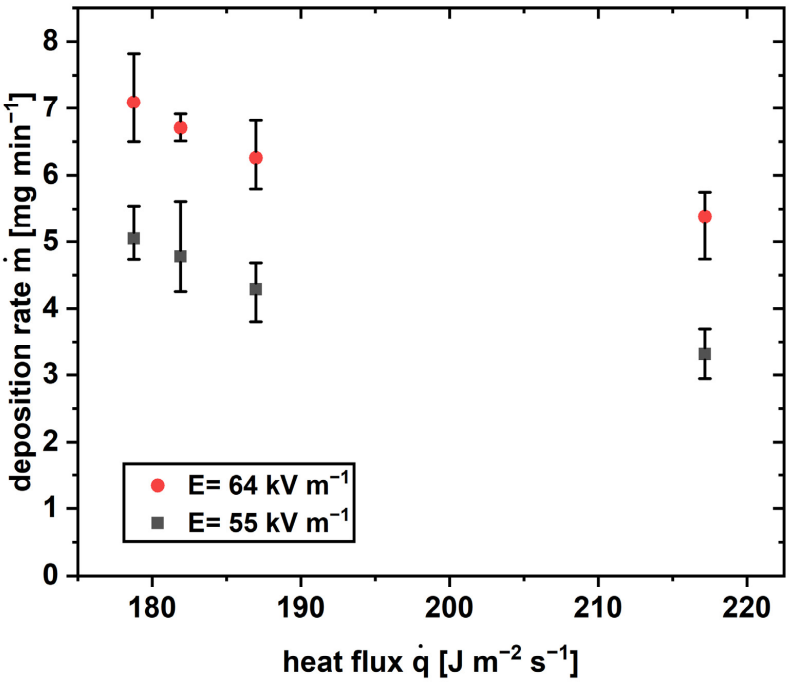

Figure 9. Deposition rate, $\dot{m}$, over the heat flux, $\dot{q}$, directed away from the heated collection electrode at two field strengths, E (av± min/max, n = 3).

For a dimensionless illustration, the relative deposition rate, $\dot{m}_{rel}$, as a ratio of the deposition rate towards the heated collection electrode, $\dot{m}_{hot}$, to the deposition rate of the cold collection electrode, $\dot{m}_{cold}$, is depicted over the Grashof number in Figure 10.

$$\dot{m}_{rel} = \frac{\dot{m}_{hot}}{\dot{m}_{cold}} \tag{25}$$

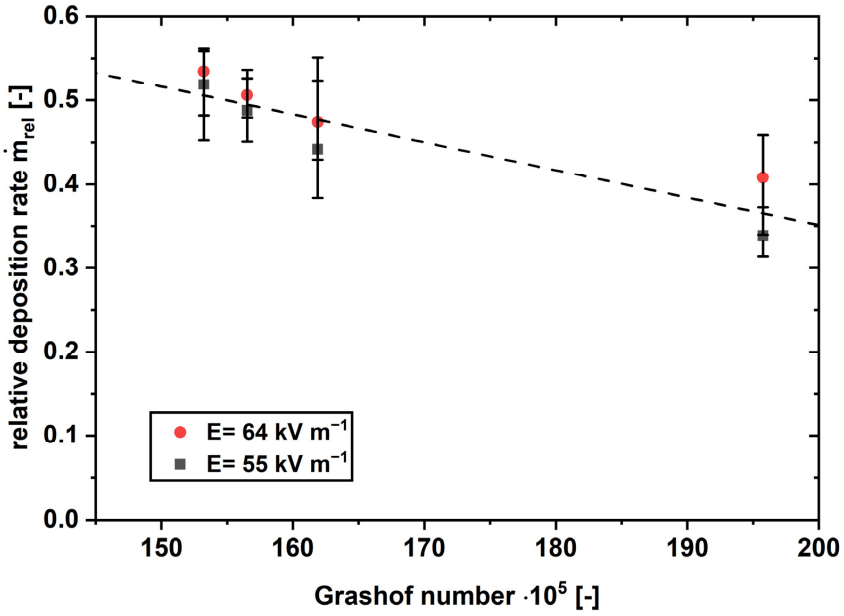

Figure 10. Relative deposition rate, $\dot{m}_{rel}$, over the Grashof number at two field strengths, E; dotted line depicts the linear correlation (av ± min/max, n = 3).

The relative deposition rate towards the collection electrode increases with a decreasing Grashof number, which means with decreasing thermal convection. The two investigated field strengths exhibit a similar behavior. The thermal effects, namely the thermophoresis and the thermal boundary layer, counteract the electrostatic force to the same extent independently of the field strength. An increase of field strength will presumably not lead to increased relative deposition rate. The relative deposition rate can be approximated by the linear correlation, $\dot{m}_{rel} = -0.003 \cdot Gr$. This observation is in agreement with the hypothesis of the thermal boundary layer hindering the particle deposition, as the thermal boundary layer increases linearly with the Grashof number [53].

3.5. Particle Deposition into a Hot Liquid

The particle deposition in a heated wall film was investigated. Molten xylitol was circulated by a pump, and drug particles (celecoxib) were deposited over a period of 8 h. Figure 10 shows the deposition rate, $\dot{m}$, towards the wall film out of molten xylitol. Particles are directly deposited into the molten xylitol so that the particle concentration in the xylitol is continuously increasing. This particle concentration is called particle mass load (wt.%) and is depicted in Figure 11.

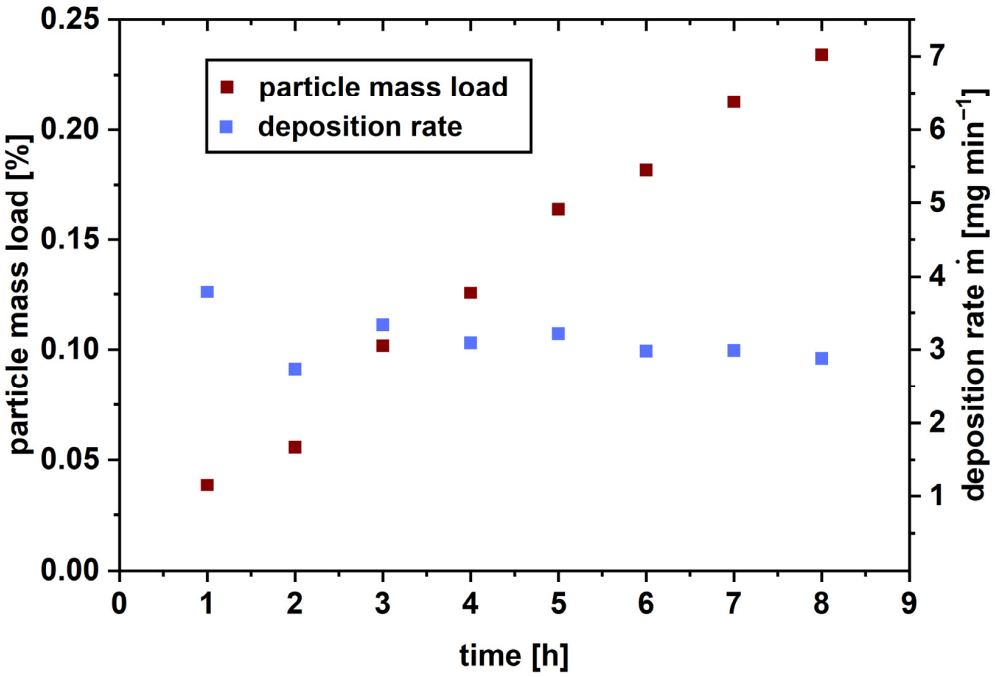

Figure 11. Particle mass load and deposition rate of celecoxib particles in molten xylitol over a period of 8 h.

A constant deposition rate towards the molten xylitol was observed. The particle mass load increased linearly over the time. Compared to another melt electrostatic precipitator, which was developed in a study before [23], the process time could be increased by a factor of 24. It is assumed that a process time above the tested 8 h will deliver constant particle deposition. The buildup of a highly resistive particle layer, which was found to be the process-time-limiting factor, is prevented by this continuously renewing wall film. The presented ESP is a meaningful tool for the continuous particle deposition and manufacturing of particle laden liquids.

3.6. In Vitro Dissolution

After particle collection into the molten xylitol, the suspension was cooled, and a solid product, a solid dispersion, was obtained. Solid dispersions consisting of a poorly water-soluble drug and a sugar alcohol are known to improve the in vitro dissolution behavior,

as it was seen in co-ground [54] and extruded formulations [24]. The main factors that lead to an increased dissolution rate are the decreased drug particle size and the increased wetting of the fine dispersed drug particles in the hydrophilic carrier [54]. In this study, the obtained solid dispersion was studied with respect to the in vitro dissolution rate in purified water (Figure 12).

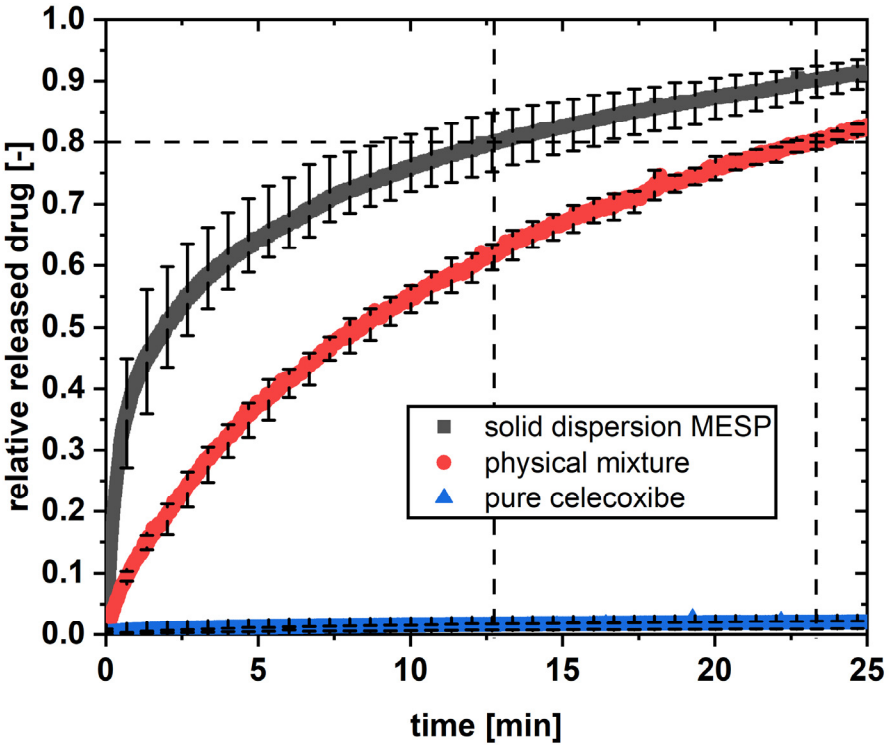

Figure 12. In vitro dissolution of celecoxib conducted in the flow-through cell with purified water at 37 °C. Dotted lines mark the time after which 80 % of drug are released in both formulations (av ± min/max, n = 3).

Pure Celecoxib exhibits a slow and incomplete dissolution over the observed period, while the physical powder mixture of celecoxib and xylitol shows a largely increased dissolution rate. A further increase in the dissolution rate was observed for the solid dispersion prepared with the ESP. A total of 80% of the celecoxib amount was dissolved from the physical mixture after 23 min, while it took only 13 min to dissolve the same amount out of the solid dispersion.

The presence of a hydrophilic, fast-dissolving carrier material surrounding the drug particle highly increases the dissolution rate of poorly soluble drugs, even for simple physical mixtures. This is probably attributable to an increased wetting of the drug particles during dissolution. The embedding of drug particles in the molten xylitol with the presented technique increases this effect even further. It is assumed that the precipitation of single particles into the molten xylitol leads to a fine dispersion of drug particles, which are entirely covered with xylitol. In this way, the drug particle surface is wetted as soon as the xylitol surrounding it is dissolved. The presented method was therefore found to be suitable for the manufacturing of solid dispersions, which exhibit a particularly fast drug dissolution. Besides the manufacturing technique, other factors also influence the drug dissolution in solid dispersions, such as particle size, drug load, the hydrodynamics in the dissolution apparatus, or the solubility of the drug in the carrier material [55,56].

4. Conclusions

The presented wet ESP is a versatile device for gentle and efficient particle recovery of even highly resistive material. Particles as valuable product can be collected for further

processing or direct transfer in a suspension. Liquid suspensions as well as solidified suspensions, as presented in this study, can be obtained. The particle collection in a hot liquid was possible, and optimum operation parameters were found. This investigation is a valuable contribution to the operation of electrostatic precipitators with hot collection electrodes. The application of a heated liquid makes the presented device superior to conventional wet ESPs.

In conclusion, this work introduces a versatile electrostatic precipitator (ESP) suitable for both dry and wet precipitation of highly resistive particles. A continuously operating prototype was designed, constructed and tested. Through the design and examination of a liquid distributer, a laminar wall film generation was achieved, highly enhancing the process time compared to a previous study (24-fold).

Studies of particle deposition on the dry, heated collection electrode demonstrated the hindrance caused by thermophoresis. Furthermore, a thermal boundary layer with an oppositely directed heat flux and the increasing drag force at higher aerosol temperatures were found to lower the particle deposition rate.

Optimum process conditions were found, and particles were successfully deposited into a heated liquid. A linear loading of molten xylitol over time was observed, proving the continuous precipitation capabilities of the ESP without the limitations of a high-resistance particle layer buildup.

A solid dispersion was prepared with this technique and the dissolution behavior was tested. A fast dissolution of the drug was found, which could be explained by improved wetting of the drug particles. The presented ESP proved to be suitable for the manufacturing of solid dispersions with beneficial dissolution properties.

Furthermore, the developed design of the ESP enables the uniform distribution of different wall film liquids across the entire distributer die, offering the flexibility to use various liquids. This versatility makes the presented ESP suitable for applications where particles need to be embedded in solid or liquid suspensions, as well as for the separation of hazardous particles to enhance safety during handling. By incorporating a heated collecting electrode, the presented ESP expands the range of applications compared to conventional ESPs. The knowledge gained from this study can be applied to improve other ESP designs, contributing to the development of electrostatic precipitators for a wide range of applications. This technology has the potential to be added to conventional spray drying equipment, relplacing the exisiting material collection systems like cyclones and filters. Using an existing spray dryer, this will reduce the investment costs and may end up in manufacuting costs like regular spray drying.

5. Patents

The melt electrostatic precipitator combined with the spray drying device, called the aerosol generator, is covered by a European patent application WO 2020/207680 A1.

Author Contributions: Conceptualization: A.J., G.S. and M.T.; methodology: A.J. and A.F.W.; investigation: A.J. and A.F.W.; writing—original draft preparation: A.J.; writing—review and editing: M.T.; visualization: A.J.; supervision: M.T.; project administration: G.S.; funding acquisition: G.S. All authors have read and agreed to the published version of the manuscript.

Funding: This project was financed by the European Regional Development Fund (EFRE- 0400356).

Data Availability Statement: The data will be available upon request from the corresponding author.

Conflicts of Interest: The authors declare no conflict of interest.

References

1. Jaworek, A.; Krupa, A.; Czech, T. Modern electrostatic devices and methods for exhaust gas cleaning: A brief review. *J. Electrost.* **2007**, *65*, 133–155. [CrossRef]
2. Mizuno, A. Electrostatic precipitation. *IEEE Trans. Dielectr. Electr. Insul.* **2000**, *7*, 615–624. [CrossRef]
3. Burger, P.; Riebel, U. Formation of highly resistive SiO_2 nanoparticle layers from the aerosol by electrostatic precipitation at 200 degrees C: Observations on back corona and nanoparticle layer structure. *J. Nanopart. Res.* **2021**, *23*, 165. [CrossRef]

4. Jaworek, A.; Czech, T.; Rajch, E.; Lackowski, M. Laboratory studies of back-discharge in fly ash. *J. Electrost.* **2006**, *64*, 306–317. [CrossRef]
5. Wang, X.; Chang, J.C.; Xu, C.Y.; Zhang, J.; Wang, P.; Ma, C.Y. Collection and charging characteristics of particles in an electrostatic precipitator with a wet membrane collecting electrode. *J. Electrost.* **2016**, *83*, 28–34. [CrossRef]
6. Chang, J.C.; Wang, P.; Cui, L.; Li, Z.Q.; Ma, C.Y.; Wang, X. Deposition characteristics of dust on wet membrane electrodes. *J. Electrost.* **2018**, *95*, 53–60. [CrossRef]
7. Bayless, D.J.; Alam, M.K.; Radcliff, R.; Caine, J. Membrane-based wet electrostatic precipitation. *Fuel Process. Technol.* **2004**, *85*, 781–798. [CrossRef]
8. Jedrusik, M.; Swierczok, A. The correlation between corona current distribution and collection of fine particles in a laboratory-scale electrostatic precipitator. *J. Electrost.* **2013**, *71*, 199–203. [CrossRef]
9. Xu, C.Y.; Chang, J.C.; Meng, Z.; Wang, X.; Zhang, J.; Cui, L.; Ma, C.Y. Wetting properties and performance test of modified rigid collector in wet electrostatic precipitators. *J. Air Waste Manag. Assoc.* **2016**, *66*, 1019–1030. [CrossRef]
10. Yang, Z.M.; Huang, C.; Ma, X.Q.; Pei, Y.K.; Sun, Y. Wetting properties and performance of modified composite collectors in a membrane-based wet electrostatic precipitator. *Open Phys.* **2019**, *17*, 897–904. [CrossRef]
11. Dey, L.; Venkataraman, C. A Wet Electrostatic Precipitator (WESP) for Soft Nanoparticle Collection. *Aerosol Sci. Technol.* **2012**, *46*, 750–759. [CrossRef]
12. Anderlohr, C.; Schaber, K. Direct Transfer of Gas-Borne Nanoparticles into Liquid Suspensions by Means of a Wet Electrostatic Precipitator. *Aerosol Sci. Technol.* **2015**, *49*, 1281–1290. [CrossRef]
13. Anderlohr, C.; Brachert, L.; Mertens, J.; Schaber, K. Collection and Generation of Sulfuric Acid Aerosols in a Wet Electrostatic Precipitator. *Aerosol Sci. Technol.* **2015**, *49*, 144–151. [CrossRef]
14. Noll, C.G. Temperature dependence of dc corona and charge-carrier entrainment in a gas flow channel. *J. Electrost.* **2002**, *54*, 245–270. [CrossRef]
15. Wang, X.H.; You, C.F. Effects of thermophoresis, vapor, and water film on particle removal of electrostatic precipitator. *J. Aerosol Sci.* **2013**, *63*, 1–9. [CrossRef]
16. You, C.F.; Wang, X.H.; Liu, R.L.; Yang, R.C. Simultaneous effects of electrostatic field and thermophoresis on inhalable particulate matter removal. *Powder Technol.* **2010**, *202*, 95–100. [CrossRef]
17. Peters, M.H.; Cooper, D.W. The Effects of Electrostatic Forces on the Thermophoretic Suppression of Particle Diffusional Deposition onto Hot Surfaces. *J. Colloid Interface Sci.* **1990**, *140*, 48–56. [CrossRef]
18. Tsai, R. A simple approach for evaluating the effect of wall suction and thermophoresis on aerosol particle deposition from a laminar flow over a flat plate. *Int. Commun. Heat Mass Transf.* **1999**, *26*, 249–257. [CrossRef]
19. Tsai, R.; Huang, J.S. Combined effects of thermophoresis and electrophoresis on particle deposition onto a vertical flat plate from mixed convection flow through a porous medium. *Chem. Eng. J.* **2010**, *157*, 52–59. [CrossRef]
20. Chen, C.L.; Chan, K.C. Combined effects of thermophoresis and electrophoresis on particle deposition onto a wavy surface disk. *Int. J. Heat Mass Transf.* **2008**, *51*, 2657–2664. [CrossRef]
21. Opiolka, S.; Schmidt, F.; Fissan, H. Combined Effects of Electrophoresis and Thermophoresis on Particle Deposition onto Flat Surfaces. *J. Aerosol Sci.* **1994**, *25*, 665–671. [CrossRef]
22. Dobrowolski, A.; Pieloth, D.; Wiggers, H.; Thommes, M. Electrostatic Precipitation of Submicron Particles in a Molten Carrier. *Pharmaceutics* **2019**, *11*, 276. [CrossRef] [PubMed]
23. Justen, A.; Kurth, C.; Schaldach, G.; Thommes, M. Preparation of Micron and Submicron Particles via Spray Drying and Electrostatic Precipitation. *Chem. Eng. Technol.* **2023**, *46*, 343–349. [CrossRef]
24. Thommes, M.; Ely, D.R.; Carvajal, M.T.; Pinal, R. Improvement of the dissolution rate of poorly soluble drugs by solid crystal suspensions. *Mol. Pharm.* **2011**, *8*, 727–735. [CrossRef] [PubMed]
25. Ziedan, H.; Tlustý, J.; Mizuno, A.; Sayed, A.; Ahmed, A. Corona current-voltage characteristics in wire-duct electrostatic precipitators, Theory versus Experiment. *Int. J. Plasma Environ. Sci. Technol.* **2010**, *4*, 154–162.
26. Kasdi, A. Computation and measurement of corona current density and V-I characteristics in wires-to-plates electrostatic precipitator. *J. Electrost.* **2016**, *81*, 1–8. [CrossRef]
27. El Dein, A.Z.; Usama, K. Experimental and simulation study of V–I characteristics of wire–plate electrostatic precipitators under clean air conditions. *Arab. J. Sci. Eng.* **2014**, *39*, 4037–4045. [CrossRef]
28. Riehle, C. Basic and theoretical operation of ESPs. *Appl. Electrost. Precip.* **1997**, 25–88. [CrossRef]
29. Andrade, R.G.S.A.; Guerra, V.G. Discharge electrode influence on electrostatic precipitation of nanoparticles. *Powder Technol.* **2021**, *379*, 417–427. [CrossRef]
30. Ning, Z.Y.; Podlinski, J.; Shen, X.J.; Li, S.R.; Wang, S.L.; Han, P.; Yan, K.P. Electrode geometry optimization in wire-plate electrostatic precipitator and its impact on collection efficiency. *J. Electrost.* **2016**, *80*, 76–84. [CrossRef]
31. Schmatloch, V.; Rauch, S. Design and characterisation of an electrostatic precipitator for small heating appliances. *J. Electrost.* **2005**, *63*, 85–100. [CrossRef]
32. Gu, Z.; Xi, X.; Yang, J.; Xu, J. Properties of RE–W cathode and its application in electrostatic precipitation for high temperature gas clean-up. *Fuel* **2012**, *95*, 648–654. [CrossRef]
33. Nusselt, W. Die oberflachenkondensation des wasserdamphes. *VDI-Zs* **1916**, *60*, 541.

34. PubChem Xylitol. Available online: https://pubchem.ncbi.nlm.nih.gov/compound/Xylitol#section=Other-Identifiers (accessed on 23 June 2023).
35. Zheng, F. Thermophoresis of spherical and non-spherical particles: A review of theories and experiments. *Adv. Colloid Interface Sci.* **2002**, *97*, 255–278. [CrossRef] [PubMed]
36. EuropeanPharmacopoeiaCommission. *European Pharmacopoeia*, 10.8th ed.; European Directorate for the Quality of Medicines: Strasbourg, France, 2022; pp. 326–373.
37. Michaeli, W. *Extrusion Dies for Plastics and Rubber: Design and Engineering Computations*, 3rd ed.; Carl Hanser Verlag GmbH Co KG: Munich, Germany, 2016; pp. 192–205.
38. Peek, F. *Dielectric Phenomena in High Voltage Engineering*, 1st ed.; McGraw-Hill: New York, NY, USA, 1929; pp. 192–237.
39. Bush, J.R.; Feldman, P.L.; Robinson, M. High temperature, high pressure electrostatic precipitation. *J. Air Pollut. Control. Assoc.* **1979**, *29*, 365–371. [CrossRef]
40. Matts, S.; Öhnfeldt, P. Efficient gas cleaning with SF electrostatic precipitators. *Flakten Rev.* **1963**, *6*, 93–110.
41. Pauthenier, M. The charge on a spherical particle in an ionized field. *J. D'physique Radium* **1932**, *7*, 590–613. [CrossRef]
42. Cochet, R. Lois charge des fines particules (submicroniques) etudes théoriques-controles récents spectre de particules. *Coll. Int. Phys. Forces Electrost. Leurs Appl. Cent. Natl. Rech. Sci. Paris* **1961**, *102*, 331–338.
43. Ishii, K.; Knioshit, M.; Kuroda, H. Dielectric-Constant Measurement on Organic Crystalline Powder. *Bull. Chem. Soc. Jpn.* **1973**, *46*, 3385–3391. [CrossRef]
44. Kothari, K.; Ragoonanan, V.; Suryanarayanan, R. Dielectric Spectroscopy of Small Molecule Pharmaceuticals—Effect of Sample Configuration. *J. Pharm. Sci.* **2014**, *103*, 3190–3196. [CrossRef]
45. Hughes, M.P.; Rosenthal, K.D.; Ran, N.A.; Seifrid, M.; Bazan, G.C.; Nguyen, T.Q. Determining the Dielectric Constants of Organic Photovoltaic Materials Using Impedance Spectroscopy. *Adv. Funct. Mater.* **2018**, *28*, 1801542. [CrossRef]
46. Schmoch, M.; Steiner, D. *Handbuch Elektrofilter*, 2nd ed.; Springer: Berlin/Heidelberg, Germany, 2022; pp. 43–80.
47. Kapitsa, P.L. *Collected Papers*, 1st ed.; Pergamon Press: Oxford, UK, 1964; pp. 662–709.
48. Al-Sibai, F. Experimentelle Untersuchung der Strömungscharakteristik und des Wärmeübergangs bei welligen Rieselfilmen. Cuvillier Verlag: Göttingen, Germany, 2006.
49. Baehr, H.D.; Stephan, K. *Wärme-Und Stoffübertragung*, 10th ed.; Springer: Berlin/Heidelberg, Germany, 2019.
50. Guha, A.; Samanta, S. Effect of thermophoresis and its mathematical models on the transport and deposition of aerosol particles in natural convective flow on vertical and horizontal plates. *J. Aerosol Sci.* **2014**, *77*, 85–101. [CrossRef]
51. Luo, R.; Li, Y.; Zheng, C.H.; Gao, X.; Fan, J.R. Numerical simulation of temperature effect on particles behavior via electrostatic precipitators. *Appl. Therm. Eng.* **2015**, *88*, 127–139. [CrossRef]
52. Li, Y.; Zheng, C.H.; Luo, K.; Gao, X.; Fan, J.R.; Cen, K.F. CFD simulation of high-temperature effect on EHD characteristics in a wire-plate electrostatic precipitator. *Chin. J. Chem. Eng.* **2015**, *23*, 633–640. [CrossRef]
53. Oprandi, A. *Fluiddynamik 2*, 1st ed.; Walter de Gruyter GmbH & Co KG: Berlin, Germany, 2020.
54. Muehlenfeld, C.; Kann, B.; Windbergs, M.; Thommes, M. Solid dispersion prepared by continuous cogrinding in an air jet mill. *J. Pharm. Sci.* **2013**, *102*, 4132–4139. [CrossRef]
55. Craig, D.Q.M. The mechanisms of drug release from solid dispersions in water-soluble polymers. *Int. J. Pharm.* **2002**, *231*, 131–144. [CrossRef]
56. Cammarn, S.R.; Sakr, A. Predicting dissolution via hydrodynamics: Salicylic acid tablets in flow through cell dissolution. *Int. J. Pharm.* **2000**, *201*, 199–209. [CrossRef]